Massive osteopetrosis caused by giant, non-functional osteoclasts in R51Q SNX10 mutant mice

Maayan Barnea,[1,9] Merle Stein,[2,9] Sabina Winograd-Katz,[3] Moran Shalev,[1] Esther Arman,[1] Ori Brenner,[4] Fadi Thalji,[5] Moien Kanaan,[6] Hila Elinav,[7] Polina Stepensky,[8] Benjamin Geiger,[3] Jan Tuckermann,[2,**] and Ari Elson,[1,*]

[1] Department of Molecular Genetics, The Weizmann Institute of Science, Rehovot 76100, Israel

[2] Institute of Comparative Molecular Endocrinology, University of Ulm, 89081 Ulm, Germany

[3] Department of Molecular Cell Biology, The Weizmann Institute of Science, Rehovot 76100, Israel

[4] Department of Veterinary Resources, The Weizmann Institute of Science, Rehovot 76100, Israel

[5] Istishari Arab Hospital, Ramallah, Palestine

[6] Hereditary Research Laboratory and Department of Life Sciences, Bethlehem University, Bethlehem, Palestine

[7] Department of Clinical Microbiology and Infectious Diseases, Hadassah-Hebrew University Medical Center, Jerusalem, Israel

[8] Department of Bone Marrow Transplantation and Cancer Immunotherapy, Hadassah-Hebrew University Medical Center, Jerusalem, Israel.

[9] These authors contributed equally to this study.

[10] Correspondence: * ari.elson@weizmann.ac.il ** jan.tuckermann@uni-ulm.de

Abstract

In this study we report on the establishment and characterization of a novel knock-in mouse model that is homozygous for the R51Q mutation in the sorting nexin 10 (SNX10) protein. This mutation leads to massive, early-onset, and widespread osteopetrosis in the mutant mice, similar to that observed in humans who are homozygous for this mutation. The diseased mice exhibit multiple additional characteristics of the corresponding human osteopetrosis, including missing and impacted teeth, occasional osteomyelitis, stunted growth, failure to thrive, and a significantly-reduced lifespan. The phenotype of homozygous R51Q SNX10 osteoclasts is unique and defines a novel form of ARO that combines both lack of bone-resorbing activity and reduced cell numbers *in vivo*. Furthermore, mutant osteoclasts grown on bone develop a giant cell morphology, reaching sizes that are up to three orders of magnitude larger than osteoclasts from wild-type or heterozygous mice. These large osteoclasts display poor survival *in vitro*, which may account for their fewer numbers *in vivo*. Electron microscopy studies indicate that homozygous mutant osteoclasts exhibit severely impaired ruffled borders and are incapable of resorbing bone, providing a clear cellular basis for the osteopetrotic phenotype. We propose that the R51Q SNX10 mutation directly causes osteoporosis by affecting both osteoclast formation and function. We further conclude that the maximal size of osteoclasts is determined by an active and genetically-regulated mechanism in which SNX10 participates, and that it is disrupted by the R51Q SNX10 mutation.

MB and MS contributed equally to this study. Correspondence should be addressed to JT or AE.

Introduction

Formation and remodeling of bone requires the coordinated activities of two cell types; osteoblasts, which deposit new bone matrix, and osteoclasts (OCLs), which degrade it. OCLs are large, multi-nucleated phagocytic cells that are generated by fusion of monocyte-macrophage precursors in a process driven by the cytokines M-CSF and RANKL. OCLs adhere to mineralized tissue via podosomes, specialized adhesion structures that assemble into a sealing zone at the cell periphery, which confines the bone area that is being degraded. The cells then secrete from a specialized region of their ventral membrane, known as the ruffled border, proteases and protons, which degrade the protein and mineral components, respectively, of the bone in the resorption cavity (1).

Proper balance between bone synthesis and degradation is critical for healthy bone homeostasis, and upsetting this balance by excessive or deficient OCL activity leads to skeletal disorders such as osteoporosis or osteopetrosis, respectively (1, 2). Of particular relevance to this study is autosomal recessive osteopetrosis (ARO; infantile malignant osteopetrosis, IMO), a cluster of genetic disorders that is caused by failure of OCL-mediated bone resorption. ARO is a rare disease, with a global incidence of 1 in 250,000 live births, and is lethal unless treated in a timely manner by hematopoietic stem cell transplantation (HSCT) that enables production of functional osteoclasts (3, 4). In most ARO cases OCLs are present but are non-functional ("osteoclast-rich ARO", (3)). Roughly two-thirds of these cases are caused by mutations in *TCIRG1*, which encodes the α3 subunit of the V0 domain of the ATP-dependent vacuolar proton pump of osteoclasts, or in *CLCN7*, which encodes chloride voltage-gated channel 7, a Cl^-/H^+ antiporter, both of which are critical for acid secretion that is essential for bone resorption by OCLs. Osteoclast-rich ARO can also arise due to mutations in *OSTM1*,which encodes the beta subunit of the Cl^-/H^+ antiporter, and *PLEKHM1*, whose lysosome-associated protein product functions in

vesicular trafficking (3-5). Osteoclast-poor ARO, caused by an absence of OCLs, has been linked to mutations in *TNFRSF11A* or *TNFSF11*, which encode the TNF receptor superfamily member 11A (RANK) or its ligand, RANKL, respectively. Both molecules are essential for differentiation of OCLs from their precursor monocytic cells (3, 4).

Homozygosity for the R51Q mutation in Sorting Nexin 10 (SNX10) was shown recently to cause ARO due to inactive OCLs in patients from Palestinian clans (6). Subsequent studies have revealed additional mutations in *SNX10,* including nonsense, mis-sense, and splicing defect mutations, that cause ARO in patients of diverse ethnic origins in Europe, North America and Asia. It is currently estimated that mutations in *SNX10* account for 5% of ARO cases globally (4, 7, 8). The specific symptoms of patients carrying distinct *SNX10* mutations vary, but several symptoms are characteristic. These include early age of onset, significantly increased bone mass, anemia, hepatosplenomegaly, and impaired vision and hearing that are caused by gradual closure of skull foramina arising from reduced bone resorption. Additional symptoms may include short stature, failure to thrive, thrombocytopenia, and absent or impacted teeth (6-8).

SNX10 belongs to a family of over 30 related proteins that participate in the regulation of endosome sorting in cells. All SNX proteins contain a phosphatidylinositol-binding (PX) domain that enables them to interact with cellular membrane compartments (9), but their exact biochemical functions are largely unknown. In addition to its N-terminal PX domain, SNX10 contains a C-terminal domain that is rich in serine residues and in negatively-charged amino acids. The function of this domain is unknown, but it appears to be required for vacuole formation in mammalian cells (10). In osteoclasts SNX10 was reported to be associated with the endoplasmic reticulum and to be present in the nucleus (11). The protein was also shown to be required for differentiation of RAW 264.7 cells into osteoclast-like cells and for their resorptive activity *in vitro* (11, 12). SNX10 associates with the ATP-dependent

vacuolar proton pump of OCLs (V-ATPase) and affects its function (13), suggesting that SNX10 might be involved in the localization of the V-ATPase to the ruffled border in OCLs (4, 6, 8).

Osteoclasts prepared *in vitro* from mononuclear leukocytes of R51Q SNX10 patients were few, grew poorly, and exhibited significantly reduced resorptive activity when cultured on mineral-coated substrates (6). Cellular studies of patients carrying the distinct Vasterbotten frameshift mutation in *SNX10* (c.212+1G>T, leading to premature termination of the protein (7)) indicated that OCLs prepared from these patients are two- to five-fold larger than cells derived from healthy individuals. The mutant OCLs are non-functional, presumably due to impaired ruffled borders (7). Global knock-down of the orthologous *Snx10* gene in mice resulted in osteopetrosis, due to reduced activity of osteoclasts, and rickets, due to elevated stomach pH and reduced calcium resorption (14). Mice in which *Snx10* was specifically knocked-down in OCLs exhibited osteopetrosis without rickets; OCLs from these mice also exhibited impaired ruffled border structure and acidification ability, and were non-functional (14).

Notably, all known mutations in SNX10 that are associated with ARO are located within the PX domain of the molecule, confirming its importance for osteoclast function. However, since the clinical manifestations of ARO induced by these mutations are variable (8), a deeper understanding of how distinct mutations affect osteoclast formation, structure, and resorption activity is needed.

In order to examine the specific consequences of the R51Q mutation in SNX10 *in vivo*, we generated R51Q SNX10 knock-in mice. We show here that homozygous R51Q SNX10 mice are severely osteopetrotic due to lack of OCL-mediated bone resorption. This and other aspects of the R51Q SNX10 mouse phenotype closely resemble the human R51Q SNX10 ARO phenotype, confirming the R51Q mutation as a causative factor for ARO. The cellular phenotype of these mice is, however, unique. R51Q SNX10 OCLs are both non-functional and less abundant *in vivo* indicating that, in contrast to other known mutations in SNX10 and in other proteins that lead to ARO, the R51Q mutation affects both the

production and the function of these cells. Homozygous R51Q SNX10 OCLs grown on bone lack ruffled borders, which abolishes their activity, and are dramatically larger than their wild-type and heterozygous counterparts, which negatively impacts their stability and survival. The gigantic size of these cells indicates that the size of OCLs is actively regulated by cellular proteins and that SNX10 plays an important role in this process, which is disrupted by the R51Q mutation.

Materials and Methods

Generation of R51Q SNX10 knock-in mice:

Mice carrying the R51Q mutation in SNX10 were constructed by CRISPR at The Weizmann Institute. Candidate sgRNA sequences were selected from SNX10 genomic sequences using sgRNAScorer 2.0 (https://crispr.med.harvard.edu/sgRNAScorer/ ;(15)) and the CRISPR design tool of the Zhang lab, MIT (http://crispr.mit.edu/). The sequence 5'-ACACCAGCAACGCGTTGCTT-3' (non-coding strand) was used. Linearized templates were transcribed with the MEGAshortscript T7 kit (sgRNA) or the mMessage Machine T7 kit (Cas9 mRNA), and purified by the MEGAclear purification kit according to the manufacturer's instructions (all from Ambion/ThermoFisher Scientific, Waltham, MA, USA). The following single-stranded DNA oligomer (non-coding strand; mutated sequence) was synthesized by Integrated DNA Technologies (Skokie, IL, USA) used for homologous recombination without purification:

*GAACTAGACTCATGGCTCCCGGTAATTTAAACTTTAAGTCACTTAC*ACCAGCAACGCGTTaCTcT

GGAGTCTTTGCCTCAGCCACACGAAtTCTCTATACCTTCTTtGTACACAAGATGTTTTCATTG

TAAAACACATGCTATTTGT*CTGTATAGAAACAGAAAAAA*

Non-italicized nucleotides are from coding sequences of exon 4 of the SNX10 gene. Shown are the guide sequence (underlined), and four mutations introduced by this oligo into genomic DNA (lowercase, underlined, in 5' to 3' order): G>A, T>C (silent mutations to prevent re-cleavage); C>T (silent, introduces an EcoRI site for genotyping); C>T (R51Q mutation).

Cas9-encoding RNA (100 ng/ul), sgRNA (50 ng/ul), and the DNA oligomer (200 ng/ul), dissolved in water, were co-injected into the cytoplasm of fertilized oocytes obtained from C57BL/6JOlaHsd mice, and the injected oocytes implanted in pseudo-pregnant foster mothers. Potential founder mice were

identified by PCR of tail biopsy DNA, and two (founders 43 and 87) were bred into independent lines by crossing with B6(Cg)-Tyr^{c-2J}/J (albino C57Bl/6J) mice. The two mutant alleles are designated by Mouse Genomic Nomenclature Committee (MGNC) as Snx10^{em1AE1} (line 43) and Snx10^{em2AE1} (line 87), but are referred to here as RQ for convenience.

Potential off-target sites for the sgRNA were selected using the CRISPR design tools of the Zhang lab, MIT (http://crispr.mit.edu/) or https://benchling.com/crispr). The five off-target sites that scored highest were selected (sequences: acagaaccaacgccttgcttcggg (Chr. 13), agaacagtaacgcgctagcttggga (Chr. 2), agtaaagcaacgctttgctttggt (Chr. 12), ataccataaacacgttgctttag (Chr. 7) and tcaccaggaagtcgttgcttaag (Chr. 13). DNA segments of 450-500 bp in length, centered around these sequences, were amplified by PCR and sequenced; no mutations were detected.

Genotyping: Genotyping by PCR was performed using oligos int3FW (5'-ACATGCCCACTGGAGTTTTC-3' and int4REV (5'-CCTGTGCCCTGTTCTTACCT-3') in a program that included of 35 cycles of denaturation (95°C, 30 seconds), annealing (58°C, 30 seconds) and elongation (72°C, 30 seconds). 1-2 microliters of unpurified product were then cut with EcoRI in a volume of 30 microliters and analyzed on a 2% agarose gel. The mutant allele yielded fragments of 387bp and 142bp, while the wild-type allele was not cut. In some cases PCR products were sequenced directly without cloning.

Animal Husbandry: At both the Weizmann Institute and at the University of Ulm, mice were housed in a barrier facility kept at 22±2°C on a light/dark cycle of 12h:12h, with food and water provided *ad libitum*. Colonies were maintained by intercrossing heterozygous (RQ/+) mice (F2 generation or beyond) to produce +/+, RQ/+, and RQ/RQ littermate mice. All pups were kept with their mothers until weaning (4 weeks), after which teeth-bearing mice (+/+, RQ/+) were separated by sex and housed up to 5 per cage. Toothless RQ/RQ mice were left to nurse up to 6-8 weeks of age, in the presence of younger litters to

ensure continued lactation. All experiments comparing mice (e.g., body weights, lengths, CTX assays) were performed on sex-matched littermate mice prior to weaning, to prevent diet-induced differences between genotypes. Primary OCLs were prepared from mice of either sex either just before or after weaning.

All experiments performed at the Weizmann Institute were approved by the Weizmann Institute IACUC (Approvals # 16810315-1, 17490415-1, 23151215-1, 26550416-3, and 38450917-3), and were conducted in accordance with Israeli law. All experiments performed at the University of Ulm were approved under animal license #1329 of the state of Baden-Württemberg and in accordance with local law.

Human Studies

Retrospective blood calcium levels from R51Q SNX10 patients were obtained from their files at the Hadassah Medical Center. Researchers conducting this study were blinded to the identity of the patients. Access to patient data was approved by the Ethics Committee of the Hadassah Medical Center and by the Institutional Review Board of The Weizmann Institute.

Primary mouse osteoclasts

Osteoclast precursors were isolated from spleens of mice aged 6-8 weeks. Spleens were washed very briefly with 70% ethanol and then in PBS, and mashed through a 70µM cell strainer into un-supplemented α-Minimal Eagle's Medium (α-MEM; Sigma, St. Louis, MO, USA). Following centrifugation, cells were resuspended for 1 minute in 1ml of red blood cell lysis buffer (Sigma), followed by addition of 10 ml unsupplemented α-MEM. Cells were seeded at a density of $5x10^6$ cells/well (for +/+ or RQ/+) and $2.5x10^6$ cells/well (RQ/RQ) in 6-well plates, or $2x10^6$ cells/well (+/+ or RQ/+) and

$1x10^6$ cells/well (RQ/RQ) in 24-well plates. Cells were cultured in complete OCL medium (α-MEM supplemented with 10% fetal calf serum, 2 mM glutamine, 50 units/ml penicillin, and 50 g/ml streptomycin, as well as 20 ng/ml M-CSF (Peprotech, Rocky Hill, NJ, USA) and 20 ng/ml RANKL (R&D Systems, Minneapolis, MN, USA)). Cells were incubated at 37 °C in 5% CO_2 for 5-7 days (day of seeding is counted as day 0) with daily changes of medium.

Culture of OCLs on bone fragments

Fragments of bovine femurs were sliced into 3X3X0.5mm slices with a low-speed diamond wheel saw, and were stored in 70% ethanol at 4°C until use. Prior to seeding, bone slices were sonicated for 10 min at 50-60 Hz, washed in 70% ethanol and in PBS, placed in 24-well plates (2-3 slices/well) and incubated in OCL medium (without cytokines) for 1hr at 37 °C in 5% CO_2. Cells were prepared as above and cultured in complete OCL medium supplemented solely with 20 ng/ml M-CSF. When confluent, cells were detached with Trypsin-EDTA and seeded at a density of $1x10^5$ Cells/well in 24-well plates or on coverslips. Cells were then cultured in complete OCL medium that included 20 ng/ml M-CSF and 20 ng/ml RANKL, with changes of medium every 48-72 hours.

Analysis of OCLs grown on bone

OCLs grown on bone slices were stained for TRAP using the Leukocyte Acid Phosphatase kit (Sigma). For actin staining, cells were permeabilized and fixed by incubating the slices in 0.5% Triton X-100/3% PFA for 3 minutes, followed by fixation in 3% PFA for 20 minutes and washes in PBS. Cells were then exposed to TRITC-phalloidin (diluted 1:500) (Sigma) for 1 hour at room temperature. DNA was visualized by incubating the slices with Hoechst 33258 (diluted 1:3000) (Molecular Probes, Eugene, OR, USA) for 3 minutes, followed by washes in PBS. For size measurements, bone fragments with OCLs

attached were collected for TRAP staining 14 (+/+) and 10 (RQ/RQ) days after the start of RANKL treatment due to the faster differentiation rate of RQ/RQ cells (Fig 5A). Cell size was measured using the ImageJ polygon tool. All multinucleated RQ/RQ cells present on two bone fragments were measured (n=280); due to their larger number, all multinucleated cells present in one field on each of two separate bone fragments were measured (n=353).

Primary mouse osteoblasts: Preparation, growth, and analysis of mineralization

Osteoblasts were prepared from calvarias of 5-day old pups and grown as described (16). For osteogenic inductions cells were seeded in 10 cm plartes at 50,000 cells/ml and induced at no more than 80% confluency the next day in culture medium (a-MEM, supplemented with 10% FCS, 100 units/ml penicillin, and 100 μg /ml streptomycin), supplemented with 100 μg/ml ascorbic acid and 1 mg/ml β-glycerophosphate, or left untreated as control. The medium was changed every 3-4 days.

After 7 days of culture early mineralization was assessed quantitatively by alkaline phosphatase (ALP) staining. ALP staining was assessed qualitatively by fixation of cells with 4% PFA and staining with Fast Violet B Salt and naphtol AS-MX phosphate alkaline solution (16). Analysis of late mineralization was performed following fixation with 4% PFA and staining with 1% Alizarin Red (pH 4.2). Quantification was carried out by measuring absorbance at 570nm after dissolving the dye with 100mM cetylpyridinium chloride.

Histomorphometry, histology, and skeletal analyses

Calcein labeling: Mice were injected IP with 30 mg/kg body weight of calcein solution (10 mg/ml calcein in 0.15M NaCl/2% $NaHCO_3$), on days 1 and 8. Mice were sacrificed on day 10; skin and internal organs were removed, and the mice were fixed in 4% paraformaldehyde/PBS for 3 days, and then kept

in 70% ethanol until analyzed. Mice were analyzed prior to weaning at 20-25 days of age; both male and female mice from both R51Q SNX10 mouse lines were analyzed.

X-ray images of mouse skeletons were obtained using an MX20 Cabinet X-Ray system (Faxitron X-Ray, Lincolnshire, IL, USA) instrument using standard settings.

Micro-CT measurements were carried out with the SkyScan1176 µCT (Bruker, Billerica, MA, USA) using a 50µm aluminum filter, 9µm voxel size and a 1° rotation step. The software programs NRecon, Data Viewer, CTAn, CTVol (Bruker) were used for analysis. For tissue mineral density measurements the bones were rehydrated in PBS and phantoms of 0.25g and 0.75g CaHA/cm^3 (Bruker) were scanned the same day for calibration.

Bone histomorphometry: Bone saples were fixed and embedded in methyl-methacrylate as described (16). Bone formation rates were measured in 8µm sections of bone after embedding in DAKO fluorescent mounting medium. For osteoblast/osteocyte analysis 5µm sections were deplasticized and stained with 0.1% toluidine blue in 0.1M sodium acetate buffer (pH 5.0). For osteocytes, the number of nuclei inside trabecular bone were counted. For osteoblasts, large square cells in contact with the bone surface and with soft edges were included in the count and their surface interface with bone marked. For von-Kossa staining sections were stained with 3% silver nitrate solution after desplastization. Sections were then treated with sodium-carbonate formaldehyde solution and sodium thiosulfate before counter staining with 0.1% safranin-O. For TRAP staining, bones were decalcified in 15% EDTA, pH 8.0, for 14 days, and then embedded in paraffin; 5µm sections were stained for TRAP using a Leukocyte Acid Phosphatase kit (Sigma-Aldrich). Slides were counterstained with hematoxylin and large, flat TRAP positive cells in contact with trabecular and cortical bone were counted. Analysis of all slides was carried using OsteomeasureXP (OsteoMetrics, Decatur, GA, USA; version 1.01)

Histology: Mouse tissues were fixed in 10% formalin, embedded in paraffin, and sectioned at 4 microns. Samples containing bone were decalcified prior to embedding. Sections were stained with Hematoxylin Solution, Gill no. 3 and with Alcoholic Eosin Y solution (Sigma), according to the manufacturer's instructions. Mice analyzed were matched for age and sex.

Bone markers in blood

CTX: Was measured using the Ratlaps CTX-1 EIA kit according to the manufacturer's instructions (IDS, Tyne and Wear, UK). Plasma samples were prepared from blood collected from the orbital sinus of 23-day old pups that had been fasting for 6 hours.

PTH: Was measured using a PTH EIA kit according to the manufacturer's instructions (Ray Biotech, Norcross, GA,USA). Plasma samples were prepared from blood collected from the orbital sinus from non-fasting 25-day old pups.

25-(OH)-vitamin D3: Was measured using the 25-(OH)-vitamin D3 kit according to the manufacturer's instructions (Enzo Biochem, New York, NY, USA). Samples were the same as those used for PTH determination.

P1NP: Was measured using the Rat/Mouse PINP EIA kit according to the manufacturer's instructions (IDS). Plasma samples were prepared from blood collected via cardiac puncture from non-fasting 5-week old male and female mice.

CTX, PTH, and 25-(OH)-vitamin D3 results were analyzed by means of four parameter logistic regression using SigmaPlot software. P1NP results were analyzed by Prism 6 software. Sex distribution of mice is noted in the relevant Figure legends.

Measurement of Gastric pH

+/+ and RQ/RQ mice, between 20-30 days old and still nursing, were of both sexes and lines. Mice were fasted for two hours and then weighed and sacrificed, and stomachs were dissected from the esophagus to the pylorus and weighed. Stomach contents were then flushed with 500 microliters of unbuffered water (pH 7.8), diluted with an equal amount of water, and the pH of the mixture was measured with a pH meter.

Electron microscopy analyses

Scanning Electron microcopy (SEM): After culturing osteoclasts on bone slices for 15-17 days as described above, cells were removed with cotton swabs and 1% bleach. The bone fragments were washed thoroughly with water 3 times, with 70% ethanol twice for 20 minutes each, and then incubated in ethanol 100% overnight. The bones were then dried in a dessicator for 24 hours, mounted on aluminum stubs, sputter-coated with iridium (CCU-010, Safematic, Bad Ragaz, Switzerland), and visualized with a Zeiss Sigma 500 scanning electron microscope (Zeiss).

Transmission electron microscopy (TEM): Bone slices carrying OCLs were fixed with 3% paraformaldehyde, 2% glutaraldehyde in 0.1 M cacodylate buffer containing 5 mM $CaCl_2$ (pH 7.4), then postfixed in 1% osmium tetroxid, stained with 2% uranyl acetate in water, dehydrated in graded ethanol solutions and embedded in Agar 100 epoxy resin (Agar Scientific Ltd., Stanstead, UK). Ultrathin sections (70-90 nm) were viewed and photographed with an FEI Tecnai SPIRIT transmission electron microscope (FEI, Eindhoven, The Netherlands), operated at 120 kV and equipped with an EAGLE CCD camera.

Protein blot analysis

Cells were washed once in PBS and lysed in RIPA buffer (50 mM Tris pH 8, 150 mM NaCl, 1% Nonidet P-40, 0.5% sodium deoxycholate, 0.1% SDS), supplemented with protease inhibitors (1 mM N-(α-aminoethyl) benzene-sulfonyl fluoride, 40 uM bestatin, 15 uM E64, 20 uM leupeptin, 15 uM pepstatin; Sigma). Protein concentrations were determined by the Bradford method using bovine serum albumin as a standard. SDS-PAGE and protein blotting were performed as described (17). Primary antibodies used included mouse monoclonal anti-actin (Sigma) and rabbit polyclonal anti-SNX10 (Sigma). Enhanced chemiluminescence signals were visualized using an ImageQuant LAS 400 Mini instrument (GE Healhtcare Biosciences, Uppsala, Sweden) and quantified (GelPro analyzer, Media Cybernetics, Rockville, MD, USA).

Quantification of Statistical Analysis

Data were analyzed by Student's t-test or the Mann-Whitney U test as indicated. Data errors (SEM, SD) are indicated in each Figure. Statistical analyses were performed using Prism 6 (GraphPad) or JMP13 (SAS). The level of statistical significance was set at $p=0.05$.

Results

Impaired growth and development in mice homozygous for the R51Q SNX10 mutation

In order to generate a pre-clinical mouse model for ARO caused by the R51Q SNX10 mutation, we mutated exon 4 of the endogenous *Snx10* gene using the CRISPR technology, in mice (Fig 1A). Two separate R51Q SNX10 mutant lines of mice were generated from independent founder mice (lines 43 and 87), and both exhibited similar phenotypes. Most of the studies below were performed in mice from line 43, with key results verified also in line 87, as indicated.

Mating of heterozygous R51Q SNX10 mice within each line yielded wild-type (+/+), heterozygous (RQ/+), and homozygous (RQ/RQ) mutant mice in near-Mendelian ratios, indicating that R51Q SNX10 does not significantly affect prenatal and early post-natal survival. Homozygous RQ/RQ mice appeared grossly normal at birth. Their weights and body lengths were similar to their wild-type and heterozygous littermates at 2 weeks of age, except for a slight decline in the weight of female RQ/RQ mice (Fig 1B). By the age of 4 weeks, a significant lag in both parameters became evident in RQ/RQ mice of both sexes (Figs 1B, 1C; Panel A in Fig S1). Internal organs, such as the liver, spleen, and stomach, were smaller in RQ/RQ mice than in RQ/+ and wild-type mice, but were in proportion with the smaller size of these mice (Panel B in Fig S1, Table S1). Upon physical examination, all RQ/RQ mice lacked teeth (Fig 1C). Histological studies revealed that molars were present but failed to erupt, and osteopetrosis was detected in most skull bones, including the maxillae and mandibles (Figs 2A, 2B). Some RQ/RQ mice developed mandibular osteomyelitis, which involved the osteopetrotic bone and surrounding soft tissues (Fig 2B). Absence of functional teeth rendered RQ/RQ pups completely dependent on mother's milk for survival; yet most of these mice appeared alert and active, despite their smaller size. RQ/RQ mice were grown routinely up to the age of 6-8 weeks in the presence of lactating females, and anecdotal experience

indicated that some can survive longer. Absence of teeth is characteristic of mice suffering from severely reduced OCL-mediated bone resorption (e.g., (18)), suggesting that the RQ/RQ phenotype is associated with OCL dysfunction. Heterozygous RQ/+ mice were physically indistinguishable from wild-type mice by all of the parameters described above.

Homozygous R51Q SNX10 mice exhibit massive osteopetrosis with mildly reduced bone mineral density

X-ray analysis revealed markedly increased density in bones from RQ/RQ mice relative to RQ/+ and wild-type mice (Fig 2C). In particular, femurs of RQ/RQ mice possessed the ARO "Erlenmeyer flask" shape (Fig 2C;(19)) that is also found in human osteopetrotic patients (3, 7). Micro-CT analysis revealed that femurs from RQ/RQ mice were shorter, deformed, and displayed a somewhat "pockmarked" appearance at the cortical bone surface; the length and cortical mineral density of these bones were reduced (Figs 2C-E; Table S2). Further examination by micro-CT revealed that the femoral bone marrow cavities of RQ/RQ mice were almost completely replaced with a compact bone matrix (Fig 3A). In line with these observations, the bone volume, trabecular thickness and number of trabeculae per unit of bone volume were significantly increased in these samples, rendering their inter-trabecular separation less apparent (Fig 3B and Table S3). Similar findings were also obtained in vertebrae (Fig 3C, Fig S2, and Table S3).

Histological analysis of the proximal tibia of RQ/RQ mice indicated massively increased amounts of trabecular bone, and corresponding reductions in bone marrow space (Figs 3D, 3E, Fig S2). Similar defects were also noted in the secondary ossification center proximal to the growth plate (Fig 3D). Significant regions of homozygous trabecular bone stained less strongly with hematoxylin/eosin (Fig 3E, Fig S2), a finding that is most likely attributable to the presence of residual, unresorbed cartilage

secondary to reduced or absent OCL activity (eg. (3)). RQ/RQ mice of both sexes were affected to similar extents, and none of the above findings were observed in RQ/+ or +/+ mice. In summary, osteopetrosis in RQ/RQ mice is widespread and affects multiple bone types, including flat bones of the skull, vertebrae, and long bones such as the tibia and femur.

It is notable that whole-body SNX10 knockdown (SNX10-KD) mice suffer from a combination of massive osteopetrosis and, paradoxically, rickets (14). While RQ/RQ mice exhibited massive osteopetrosis and their bone mineral density was somewhat reduced (Table S2), their gastric pH, stomach appearance, and circulating levels of calcium and PTH were normal (Fig 3F, Table S1, and Fig S3). The stomach weights of these mice were in proportion to their body weight (Table S1), collectively indicating that dietary calcium resorption is normal. RQ/RQ mice exhibited reduced levels of circulating 25(OH)-Vitamin D (+/+: 14.25+2.43 ng/ml (n=31 mice); RQ/RQ: 6.97+2.24 ng/ml (n=16 mice); p=0.021), which explains their reduced bone mineral density; the reasons for reduced vitamin D levels are unknown. Of note, ARO patients in which the disease is caused by the R51Q SNX10 mutation exhibit normal values of circulating calcium (Fig 3F), and there are no reports of them suffering from rickets. We conclude that RQ/RQ mice suffer from massive and widespread osteopetrosis that is similar to the major clinical symptoms of ARO caused by R51Q SNX10 in humans.

Decreased OCL numbers in RQ/RQ mice

OCL numbers in bones of RQ/RQ mice were significantly reduced; fewer TRAP-positive OCLs were visible in histological samples of mutant bone (Fig 4A), as well as when OCL numbers were quantified by bone histomorphometric analysis (Fig 4B, Table S4). Homozygous bone samples contained normal numbers of osteocytes (Fig 4C, Table S4) but, unexpectedly, reduced numbers of osteoblasts (OBs; see Fig 4D; Table S4). However, bone formation rates were normal in RQ/RQ mice (Fig 4E),

indicating that the phenotype of these mice is not due to a major bone formation defect. This conclusion is further supported by the finding that OBs derived from calvarias of +/+, RQ/+, and RQ/RQ mice exhibited similar mineralization rates *in vitro* (Fig S4). Plasma levels of N-terminal type-I procollagen (P1NP), a marker of bone formation *in vivo*, were not distinct in RQ/RQ mice vs. controls (Fig 4F).

Of note, RQ/RQ mice displayed elevated levels of plasma collagen type-I cross-linked C-telopeptides (CTX) (Fig 4G), which is used as a clinical indicator of OCL-mediated bone resorption *in vivo*. Elevated CTX levels contradict the massive increase in bone mass found in RQ/RQ mice by several independent methodologies, and, critically, the absent ability of RQ/RQ OCLs to degrade bone (see below). We note that CTX levels can be affected also by other parameters, such as clearance rates (20). Moreover, high CTX levels *in vivo* despite reduced OCL activity have been documented in various mouse models of OCL dysfunction as discussed further below.

RQ/RQ osteoclasts are gigantic

In humans, the cause of ARO induced by the R51Q SNX10 mutation is aberrant OCL-mediated bone resorption (6). Absence of teeth (Fig 1C), reduced OCL numbers in femurs (Figs 4A, 4B), and presence of massive osteopetrosis despite normal bone formation rates (Fig 4E) suggest that OCL activity is reduced in RQ/RQ mice *in vivo*. The significant reduction in the bone marrow volume in RQ/RQ mice led us to generate OCLs *in vitro* by culturing primary splenocytes in the presence of M-CSF and RANKL. Cells from RQ/RQ mice adhered to bone and grew rapidly, fusing to form massive multinuclear cells that were dramatically larger than similar cells from +/+ or from RQ/+ mice (Figs 5A, 5B, 5D). These large RQ/RQ OCLs stained positively for TRAP, but staining was less intense and more diffuse than that seen in wild-type or RQ/+ cells (Fig 5A). RQ/RQ OCLs grown on bone grew, and then fused and died before their matched +/+ and RQ/+ counterparts (Fig 5A). RQ/RQ OCLs each

exhibited a single sealing zone structure that demarcated the entire periphery of the cell, in proportion with its size, in contrast to the much smaller sealing zone structures of +/+ and RQ/+ OCLs (Fig 5B).

In order to compare their bone resorptive capacity, we seeded +/+, RQ/+, and RQ/RQ splenocytes on fragments of bovine bone and grew them for 15 days in the presence of M-CSF and RANKL. Cells from all three genotypes grew well and fused as indicated in Fig 5A. We then removed the cells and examined the formation of resorption pits on the bone surface, which indicate OCL activity, by scanning electron microscopy (SEM). As seen in Fig 5C, OCLs from +/+ and RQ/+ mice readily formed resorption pits that were similar in size and in appearance. In contrast, RQ/RQ OCLs did not form pits at all, indicating they are severely deficient in function. Since the pit resorption assay provides an accumulated record of resorption activity throughout the life of the culture, these results also indicate that the RQ/RQ cells were at no time capable of significant activity.

Measurements of the areas of individual OCLs grown on bone fragments indicated that the average size of RQ/RQ OCLs was 14.6 times larger than +/+ OCLs; this ratio increased to 49 when the largest 5% of cells of each genotype were compared (Fig 5D). RQ/RQ cultures contained a significant number of cells that reached sizes more than 100-fold larger than the average +/+ OCL (Fig 5D). No cells of similar size were observed in +/+ or RQ/+ cultures.

We next examined if the R51Q mutation affects expression of the SNX10 protein *in vivo*. Protein blots prepared from mouse OCLs revealed that the SNX10 protein is expressed at relatively low levels in macrophages produced following M-CSF treatment of splenocytes, but its expression is significantly increased upon RANKL-induced differentiation of these cells into OCLs. This expression pattern is observed in +/+, RQ/+, and RQ/RQ cells (Fig 5E). OCLs from mice of the three genotypes express similar levels of the SNX10 protein (Fig 5E), indicating that the R51Q mutation does not affect overall SNX10 protein levels. Importantly, +/+ OCLs express wild-type *Snx10* mRNA, and RQ/RQ

OCLs express mutant mRNA exclusively; OCLs from RQ/+ mice express both *Snx10* mRNA species (Fig S5). Taken together, the expression of mutant SNX 10 RQ/RQ in maturing osteoclasts leads to apparently deregulated fusion and increased size of osteoclasts.

RQ/RQ osteoclasts exhibit abnormal ruffled borders and are severely functionally impaired

We next examined the structure of RQ/RQ OCLs grown on bone *in vitro* by transmission electron microcopy (TEM). Ruffled borders, the basal membranal structures through which the cells secrete acid and proteases onto the bone surface below, were present in all +/+ and RQ/+ cells, visible as areas in which heavily convoluted membranous folds extended from the ventral aspect of the cells onto and into the bone surface below (Fig 6A). In contrast, RQ/RQ OCLs lacked ruffled border structures. Some cells did not appear to make contact with bone, while others made contact with bone via a nearly flat surface that completely lacked the convoluted structure of the ruffled border membranes (Fig 6A). TEM was also used to examine the structure of endogenous OCLs in femurs of +/+ and RQ/RQ mice. Here, too, convoluted membranal structures typical of ruffled borders were observed in +/+ cells (Fig 6B), while RQ/RQ OCLs lacked ruffled borders or made contact with the underlying bone surface through surfaces that did not resemble the ruffled border seen in +/+ cells (Fig 6B). Our results indicate that the massive osteopetrosis of R51Q SNX10 mice arises from virtual lack of OCL-mediated bone resorption that is caused by absent or dysfunctional ruffled border structures.

Discussion

Autosomal recessive osteopetrosis is a lethal genetic disease, whose main symptoms are caused by OCL dysfunction. The only treatment currently available for ARO is hematopoietic stem cell transplantation (HCST), which enables production of healthy and functional OCLs that restore bone resorbing abilities and prevent further bone-associated symptoms. HSCT is a difficult procedure, and is offered in cases where all of the patient's symptoms are caused by OCL dysfunction. This typically precludes HCST as a treatment for patients whose underlying mutation causes significant additional, eg. neurological, complications (3, 21, 22). Moreover, HCST does not reverse all the damage caused by absent bone resorption, such as losses of hearing and vision that are caused by closure of skull foramina. These facts, together with the rare occurrence of ARO and its heterogeneous genetic basis, make development of accurate mouse model systems for ARO essential to clarify its cellular and molecular underpinnings, and to provide alternative approaches for diagnosis and therapy.

In order to further these goals we have produced mice that carry the R51Q mutation in SNX10, the first mutation in SNX10 suggested to cause ARO in humans (6). Homozygous R51Q SNX10 mice exhibit multiple phenotypes that are present also in humans suffering from ARO. A key feature among these is massive, early-onset, and widespread osteopetrosis that is caused by dysfunctional OCLs. Additional similarities include the "Erlenmeyer flask" shape of the distal femoral metaphysis, dental defects (missing and impacted teeth), occasional osteomyelitis, stunted growth, failure to thrive, and a significantly reduced lifespan (3, 21, 22). Hepatosplenomegaly and anemia, which often develop in ARO patients, were not found in RQ/RQ mice, possibly due to their short lifespan that precludes development of these symptoms. These findings confirm the R51Q mutation in SNX10 as a causative factor in ARO.

A prominent feature of RQ/RQ OCLs is their size; these cells grow to become dramatically larger than wild-type OCLs, which are large cells in their own right. The size phenotype is likely cell-autonomous since it is detected after several days of differentiation *ex vivo* in culture, and occurs irrespective of the tissue origin of the OCL precursor cells or of their growth surface. The mechanism underlying this phenotype remains unclear but might include, for example, increased fusion of precursor cells or excess spreading and flattening of the multi-nuclear fusion products. Importantly, these findings indicate that the enigmatic mechanism that regulates OCL size is actively regulated by cellular-genetic mechanisms, in which SNX10 plays a central role and which is disrupted by the R51Q mutation.

Another striking feature of RQ/RQ OCLs is their inability to resorb bone *ex vivo*, a finding that accounts for the massive osteopetrosis of RQ/RQ mice. The inability of RQ/RQ OCLs to resorb bone is most likely the result of structurally-defective or absent ruffled borders, which are essential for proper OCL activity. Ruffled borders are composed of large, elaborate membranal folds that emanate from the ventral side of the cell. SNX10 and other SNX family members participate in the sorting of cellular vesicles, a process that involves cellular membranes and can affect their structure. It is possible that the R51Q SNX10 mutation disrupts membranal sorting in a manner that prevents proper development and function of the ruffled border. The large size of RQ/RQ OCLs may also contribute to their loss of function. For example, the strikingly larger size of the sealing zone structures of RQ/RQ OCLs (Fig 5B) may make it difficult to isolate a particular area of bone surface, prior to its intended degradation. The large size of RQ/RQ OCLs may also diminish their survival, in agreement with their increased fragility and significantly shorter lifespan *in vitro* (Fig 5A) and with their reduced numbers *in vivo* (Fig 4A, 4B).

Serum CTX levels, which are considered a clinical indicator of OCL-mediated bone resorption *in vivo,* are elevated in RQ/RQ mice. This finding appears to contradict the documented inactivity of RQ/RQ OCLs and the massively increased bone mass of these mice in the presence of normal bone formation

rates. However, serum CTX levels in osteopetrotic mouse models vary considerably, from reduced (e.g., in mice lacking RANKL(23) or Rac (24)), through unchanged (e.g., mice lacking Src, (23)) to increased (e.g., mice lacking CLCN-7 (25) or in SNX10-KD mice (14)). In cases of osteoclast-rich disease, minimal resorptive activity of OCLs coupled with their high absolute numbers, such as in CLCN-7-deficient mice (25), have been suggested to account for elevated CTX levels. However, RQ/RQ mice contain fewer OCLs per unit surface area of bone, arguing against the validity of this explanation in this case. High CTX levels might also be caused by disruption of processes unrelated to bone, such as increased stability of CTX peptides or their reduced clearance rates from the circulation (20).

Two major types of ARO have been described in humans and in mouse models for this disease: OCL-poor ARO, which is caused by mutations in gene products that are essential for production of OCLs, and OCL-rich disease, in which normal or increased amounts of functionally-impaired OCLs are present due to mutations that affect vesicle trafficking and ruffled border formation, but not cell production or survival (3). The R51Q SNX10 mutation defines a third category, in which OCLs are both non-functional and their amount is significantly reduced *in vivo*. We believe that the basis for this unique phenotypic combination are the dual consequences of the R51Q mutation in SNX10, which renders the cells inactive while increasing their size to a degree that reduces their survival *in vivo*.

SNX10-KD mice have also been proposed as a model for ARO (14). While osteopetrosis and other major parts of the RQ/RQ phenotype are also found in SNX10-KD mice, significant differences exist between these models. The SNX10-KD mouse phenotype is characterized by an increased mass of bone that exhibits, paradoxically, markedly reduced mineral content (14). This rachitic phenotype is likely due to disruption of SNX10 function in the stomach that leads to higher gastric pH, abnormal stomach appearance, and reduced absorption of dietary calcium (14). The femoral mineral content of RQ/RQ mice is reduced, but to a lesser degree than that seen in SNX10-KD mice. Moreover, the main defects that

give rise to the rachitic phenotype of SNX10-KD mice do not exist in RQ/RQ mice: stomach appearance and gastric pH are normal, as are serum levels of PTH and, critically, calcium. The somewhat decreased mineral density in RQ/RQ bones is therefore not caused by decreased bioavailability of dietary calcium, but might be due to the reduced levels of vitamin D3 in circulation that likely arise by an unrelated mechanism. We note that normal concentrations of circulating calcium were reported in humans suffering from ARO induced by R51Q SNX10 (Fig 3F) and by the Vasterbotten frameshift mutation in SNX10 [10]; rickets symptoms were not reported in these cases (6, 7). Administering calcium gluconate, which bypassed reduced calcium resorption in the SNX10-KD mice and resolved their rachitic phenotype (14), is therefore not a general treatment for all forms of SNX10-based ARO, and its potential benefit most likely depends on the identity of the SNX10 mutation at hand.

OCLs two to five times larger than controls have been reported in cultures prepared from blood monocytes of patients of the genetically-distinct SNX10 Vasterbotten variant of ARO (7), and in mice lacking OSTM-1 (26) that model another cause of ARO. We note that large OCLs were not described in mice carrying whole-body or OCL-specific knockdowns of SNX10 (14). Since knockdown efficiency in the latter SNX10 models was high but nonetheless not complete, it is possible that residual amounts of WT SNX10 protein were sufficient to maintain normal OCL sizes. Alternatively, the size differences between R51Q SNX10 and SNX10-KD OCLs may reflect a true distinction between the consequences of reduced expression of wild-type SNX10 vs. normal expression levels of its R51Q mutant. In either case, these size differences provide further indication that different mutations in SNX10 can result in distinct phenotypes.

Data presented in this study indicate that the osteopetrotic phenotype of RQ/RQ mice is caused by a significant loss of function by OCLs. It is, however, less clear how the R51Q mutation affects the as-yet unknown biochemical functions of the SNX10 protein within these cells. RQ/+ mice that are

heterozygous for the R51Q SNX10 mutation are indistinguishable from +/+ mice. This fact, together with the normal size, ruffled border morphology, and *ex-vivo* resorbing activity of RQ/+ OCLs indicates that heterozygosity for R51Q SNX10 does not elicit OCL or bone phenotypes. It is therefore highly unlikely that the R51Q SNX10 mutant protein acts through a dominant gain-of-function mechanism. It possible that R51Q SNX10 acts by a loss-of-function mechanism, or by a gain-of-function mechanism that becomes evident only in the absence of the wild-type protein. The former explanation is challenged by the differences between the R51Q SNX10 and SNX10 knockdown (SNX10-KD) mouse models at the whole-animal and cellular levels that were described above.

Multiple mutations in SNX10 have now been described in ARO (6-8). Our study underscores the importance of mimicking the human mutations as closely as possible in preclinical models, since loss-of-function approaches do not necessarily generate the complex phenotypes seen at the cellular level and prevent examination of possible gain-of-function effects of these mutations. By presenting one of the first knock-in models for ARO, we accomplish this aim for the SNX10 R51Q mutation and establish a valuable tool for uncovering mechanisms of this genetic disorder for the future development of more effective therapeutic strategies.

Supplemental Data

Supplemental data include five figures and four tables.

Declaration of Interests

The authors declare no competing interests.

Acknowledgements

We thank Dr. Timothy Dahlem and the University of Utah Mutation Generation and Detection Core Facility for reagents. We also thank Dr. Rebecca Haffner-Kraus, Ms. Golda Damari, Dr. Alina Berkovitz, and Ms. Sima Peretz of the Weizmann Institute's Transgenic and Knockout Core Facility for help in preparing the mouse models used in this study; Ms. Ofira Higfa, Mr. Neriah Sharabi and Mr. Thomas Neidlinger for expert animal care in the central animal facilities of the Weizmann Institute and Ulm University; and Dr. Elena Kartvelishvily, Dr. Smadar Zaidman, and Ms. Ilana Sabanay of the Weizmann Institute's Chemical Research Support Department for assistance with electron microscopy studies. We also thank Prof. Memet Aker for discussions at the start of this project. This study was supported by a grant from the Trilateral program of the Deutsche Forschungsgemeinschaft (Germany) (to BG, JT, AE, MK, and FT, Tu220/12), and by the Kekst Family Institute for Medical Genetics and the David and Fela Shapell Family Center for Genetic Disorders Research, both of The Weizmann Institute of Science (to AE and BG). AE is the incumbent of the Marshall and Renette Ezralow Professorial Chair. BG is the Erwin Neter Professor in Cell and Tumor Biology.

References

1. Novack, D. V., and Teitelbaum, S. L. (2008) The osteoclast: friend or foe? *Annu Rev Pathol* **3**, 457-484
2. Bruzzaniti, A., and Baron, R. (2006) Molecular regulation of osteoclast activity. *Rev Endocr Metab Disord* **7**, 123-139
3. Sobacchi, C., Schulz, A., Coxon, F. P., Villa, A., and Helfrich, M. H. (2013) Osteopetrosis: genetics, treatment and new insights into osteoclast function. *Nat Rev Endocrinol* **9**, 522-536
4. Palagano, E., Menale, C., Sobacchi, C., and Villa, A. (2018) Genetics of Osteopetrosis. *Curr Osteoporos rep* **16**, 13-25
5. Del Fattore, A., Cappariello, A., and Teti, A. (2008) Genetics, pathogenesis and complications of osteopetrosis. *Bone* **42**, 19-29
6. Aker, M., Rouvinski, A., Hashavia, S., Ta-Shma, A., Shaag, A., Zenvirt, S., Israel, S., Weintraub, M., Taraboulos, A., Bar-Shavit, Z., and Elpeleg, O. (2012) An SNX10 mutation causes malignant osteopetrosis of infancy. *J Med Genet* **49**, 221-226
7. Stattin, E. L., Henning, P., Klar, J., McDermott, E., Stecksen-Blicks, C., Sandstrom, P. E., Kellgren, T. G., Ryden, P., Hallmans, G., Lonnerholm, T., Ameur, A., Helfrich, M. H., Coxon, F. P., Dahl, N., Wikstrom, J., and Lerner, U. H. (2017) SNX10 gene mutation leading to osteopetrosis with dysfunctional osteoclasts. *Sci Rep* **7**, 3012, doi:3010.1038/s41598-41017-02533-41592
8. Pangrazio, A., Fasth, A., Sbardellati, A., Orchard, P. J., Kasow, K. A., Raza, J., Albayrak, C., Albayrak, D., Vanakker, O. M., De Moerloose, B., Vellodi, A., Notarangelo, L. D., Schlack, C., Strauss, G., Kuhl, J. S., Caldana, E., Lo Iacono, N., Susani, L., Kornak, U., Schulz, A., Vezzoni, P., Villa, A., and Sobacchi, C. (2013) SNX10 mutations define a subgroup of human autosomal recessive osteopetrosis with variable clinical severity. *J Bone Miner Res* **28**, 1041-1049
9. Cullen, P. J. (2008) Endosomal sorting and signalling: an emerging role for sorting nexins. *Nat Rev Mol Cell Biol* **9**, 574-582
10. Qin, B., He, M., Chen, X., and Pei, D. (2006) Sorting nexin 10 induces giant vacuoles in mammalian cells. *J Biol Chem* **281**, 36891-36896
11. Zhu, C. H., Morse, L. R., and Battaglino, R. A. (2012) SNX10 is required for osteoclast formation and resorption activity. *J Cell Biochem* **113**, 1608-1615
12. Zhou, C., Wang, Y., Peng, J., Li, C., Liu, P., and Shen, X. (2017) SNX10 plays a critical role in MMP9 secretion via JNK-p38-ERK signaling pathway. *J Cell Biochem* **118**, 4664-4671
13. Chen, Y., Wu, B., Xu, L., Li, H., Xia, J., Yin, W., Li, Z., Shi, D., Li, S., Lin, S., Shu, X., and Pei, D. (2012) A SNX10/V-ATPase pathway regulates ciliogenesis in vitro and in vivo. *Cell Res* **22**, 333-345
14. Ye, L., Morse, L. R., Zhang, L., Sasaki, H., Mills, J. C., Odgren, P. R., Sibbel, G., Stanley, J. R., Wong, G., Zamarioli, A., and Battaglino, R. A. (2015) Osteopetrorickets due to Snx10 deficiency in mice results from both failed osteoclast activity and loss of gastric acid-dependent calcium absorption. *PLoS Genet* **11**, e1005057
15. Chari, R., Mali, P., Moosburner, M., and Church, G. M. (2015) Unraveling CRISPR-Cas9 genome engineering parameters via a library-on-library approach. *Nat Methods* **12**, 823-826
16. Liu, P., Lee, S., Knoll, J., Rauch, A., Ostermay, S., Luther, J., Malkusch, N., Lerner, U. H., Zaiss, M. M., Neven, M., Wittig, R., Rauner, M., David, J. P., Bertolino, P., Zhang, C. X., and

Tuckermann, J. P. (2017) Loss of menin in osteoblast lineage affects osteocyte-osteoclast crosstalk causing osteoporosis. *Cell Death Differ* **24**, 672-682
17. Gil-Henn, H., and Elson, A. (2003) Tyrosine phosphatase-epsilon activates Src and supports the transformed phenotype of Neu-induced mammary tumor cells. *J Biol Chem* **278**, 15579-15586
18. Soriano, P., Montgomery, C., Geske, R., and Bradley, A. (1991) Targeted disruption of the c-src proto-oncogene leads to osteopetrosis in mice. *Cell* **64**, 693-702
19. Faden, M. A., Krakow, D., Ezgu, F., Rimoin, D. L., and Lachman, R. S. (2009) The Erlenmeyer flask bone deformity in the skeletal dysplasias. *Am J Med Genet A* **149a**, 1334-1345
20. Vasikaran, S., Eastell, R., Bruyere, O., Foldes, A. J., Garnero, P., Griesmacher, A., McClung, M., Morris, H. A., Silverman, S., Trenti, T., Wahl, D. A., Cooper, C., and Kanis, J. A. (2011) Markers of bone turnover for the prediction of fracture risk and monitoring of osteoporosis treatment: a need for international reference standards. *Osteoporos Int* **22**, 391-420
21. Wu, C. C., Econs, M. J., DiMeglio, L. A., Insogna, K. L., Levine, M. A., Orchard, P. J., Miller, W. P., Petryk, A., Rush, E. T., Shoback, D. M., Ward, L. M., and Polgreen, L. E. (2017) Diagnosis and Management of Osteopetrosis: Consensus Guidelines From the Osteopetrosis Working Group. *J Clin Endocrinol Metab* **102**, 3111-3123
22. Tolar, J., Teitelbaum, S. L., and Orchard, P. J. (2004) Osteopetrosis. *N Engl J Med* **351**, 2839-2849
23. Takeshita, S., Fumoto, T., Ito, M., and Ikeda, K. (2017) Serum CTX levels and histomorphometric analysis in Src versus RANKL knockout mice. *J Bone Miner Metab*
24. Zhu, M., Sun, B. H., Saar, K., Simpson, C., Troiano, N., Dallas, S. L., Tiede-Lewis, L. M., Nevius, E., Pereira, J. P., Weinstein, R. S., Tommasini, S. M., and Insogna, K. L. (2016) Deletion of Rac in Mature Osteoclasts Causes Osteopetrosis, an Age-Dependent Change in Osteoclast Number, and a Reduced Number of Osteoblasts In Vivo. *J Bone Miner Res* **31**, 864-873
25. Neutzsky-Wulff, A. V., Karsdal, M. A., and Henriksen, K. (2008) Characterization of the bone phenotype in ClC-7-deficient mice. *Calcif Tissue Int* **83**, 425-437
26. Pata, M., and Vacher, J. (2018) Ostm1 bifunctional roles in osteoclast maturation: insights from a mouse model mimicking a human OSTM1 mutation. *J Bone Miner Res*

Figure Legends

Fig 1: R51Q knock-in mice are growth-retarded.

(A) Top: Scheme of the *Snx10* gene and location of the R51Q mutation (asterisk). Open boxes: Non-coding exon segments; not drawn to scale. Middle: Genotyping of mice by tail biopsy PCR (+/+: wild type; RQ/+: heterozygous; RQ/RQ: homozygous mutant). Bottom: Sequence from tail biopsy DNA documenting the mutation. The mutant nucleotide is indicated by an arrow; sequence shown is anti-sense. **(B)** Body weights of mice at 2 and 4 weeks of age. Shown are means±SD, n=7-22 mice/bar. *: $p=0.048$ vs WT. **: $p\leq0.0022$ vs +/+ or RQ/+. ***: $p\leq2.3\times10^{-6}$vs. +/+ or RQ/+ by Student's t-test. Data is from lines 43 and 87. **(C)** RQ/RQ mice are shorter than matched +/+ controls and lack teeth. Male mice aged 5 weeks are shown.

Fig 2: Effect of Snx10 R51Q on bone shape and mineralization.

(A) Coronal section through RQ/RQ mouse head showing osteopetrosis of the zygomatic arch (upper box) and penetrating mandibular osteomyelitis (lower box). M: Impacted molars; O: Osteomyelitis and cellulitis; T: Tongue; Z: Zygomatic arch. Scale bar: 1,000 µm. **(B)** Enlarged images of boxed regions in Panel A, compared with +/+ controls. Top: Osteopetrosis of the Zygomatic arch. Arrowheads mark examples of osteopetrotic bone (RQ/RQ) vs. normal bone (+/+). Bottom: Mandibular osteomyelitis and cellulitis. In: Incisor (ectopic in RQ/RQ); M: Molar (impacted in RQ/RQ). O: Osteomyelitic region. Arrows mark osteopetrotic and inflamed mandibular bone and adjacent soft tissue (RQ/RQ) vs. normal mandible (+/+). Scale bars: 500 µm. Images shown are representative of 4 RQ/RQ and 4 +/+ mice, age 5-8 weeks. **(C)** Mouse whole skeleton X-ray (left, middle) and 3D femur reconstruction by µCT (right), showing abnormal "Erlenmeyer flask" shape and higher radiodensity (arrow) with severely reduced marrow cavity volume in RQ/RQ mice. Mice shown are females aged 5 weeks. **(D)**

RQ/RQ mice display shorter femora than matched +/+ controls at 5 weeks. Femur length was measured from head to condyli. Shown are means±SD, n=3-5 mice/bar; $p \leq 0.05$ by Mann Whitney-U test. **(E)** Tibial tissue mineral density (TMD) was determined by μCT, via normalization to CaHA phantoms of known density. Shown are means±SD, n=3-5 mice/bar; $p \leq 0.05$ by Mann Whitney-U test.

Fig 3: Structure of bones from homozygous R51Q SNX10 mice.

(A) Frontal plane section of tibiae from +/+, RQ/+, and RQ/RQ mice by micro-CT. Note nearly complete absence of bone marrow cavity in the homozygous sample. **(B)** Key histomorphometric parameters of cancellous bone in femora of male mice aged 5 weeks. Data are mean+SD; n=3-5 mice/bar. *: $p<0.001$ by Mann-Whitney U test. BV/TV: Bone volume relative to total volume measured. Tb.Th: Trabecular thickness. Tb.N: Number of trabeculae. Tb.Sp: Trabecular separation. See Table S3 for complete data. **(C)** μCT examination of vertebrae, showing increased bone mass and radiodensity in RQ/RQ samples. See Table S3 for histomorphometric data **(D)** von Kossa-stained section of tibia from +/+ and RQ/RQ mice. Scale bar: 1 mm. **(E)** Similar to D stained with hematoxylin-eosin, showing magnified view of trabecular bone from a region distal to the growth plate. Arrow denotes unresorbed cartilage. Scale bar: 100μm. **(F)** Serum calcium levels in 12 human SNX10 R51Q patients (each bar represents means±SD of repeated measurements of an individual patient over a period of several months). Gray background band shows the healthy laboratory reference range, indicating that all patients exhibit normal values. Right: Snx10 RQ/RQ mice exhibit normal serum calcium levels (n=9-10 mice per genotype, aged 3 weeks).

Fig 4: Bone formation and resorption in R51Q SNX10 mice.

(A) Femur sections from +/+ and homozygous RQ/RQ mice stained for tartarate-resistant acid phosphatase (TRAP, purple, stains OCLs), and counterstained with hematoxylin. Scale bar: 0.1 mm. Bottom: Magnified view of boxed regions in top panels. Scale bar: 20 μm. Note reduced OCL numbers in mutant samples. **(B)** Histomorphometric quantification of bone surface area in contact with OCLs (Oc.S/BS). *: $p \leq 0.05$ by Mann-Whitney U test. n=3-5 mice aged 5 weeks per bar. **(C)** Histomorphometric quantification of the number of osteocytes per unit bone area (N.Ot/B.Ar). **(D)** Similar to B, for osteoblasts. *: $p \leq 0.05$, by Mann-Whitney U test. **(E)** Left: Cortical bone formation rate. Right: incorporation of calcein into bone following two calcein injections 8 days apart. Scale bar: 10 μm. **(F)** Plasma concentrations of N-terminal type-I procollagen (P1NP). n=3-5 mice aged 5 weeks per bar. **(G)** Plasma concentrations of collagen type-I cross-linked C-telopeptides (CTX). n=11-25 mice age 21-26 days per bar. $p \leq 0.011$ by Student's t-test. All data shown are Mean±SD.

Fig 5: Giant osteoclasts from R51Q SNX10 homozygous mice.

Spleen cells from +/+, RQ/+, and RQ/RQ mice were seeded on slices of bovine bone and grown in the presence of M-CSF and RANKL for up to 15 days. **(A)**. Bone fragments were stained for TRAP on the indicated days. Scale bars: 200 μm. Image of RQ/RQ cells at day 12 is a composite of two identical pictures taken at different focal planes to account for unevenness of the bone surface. **(B)** Cells were stained with phalloidin (yellow; indicating actin in sealing zones) and Hoechst 33258 (blue; indicating DNA in nuclei). Top: Scale bar: 100 μm. Note that most of the RQ/RQ image is occupied by two giant cells; the areas they cover are marked with one or two asterisks, respectively. Each figure in this panel is a composite of 15 smaller contiguous fields. Boxes indicate regions magnified at the right. Right: Magnified views; asterisk in RQ/RQ image indicates a region within a single OCL. Scale bar: 50 μm.

(C) RQ/RQ OCLs are inactive. SEM images of bone fragments seeded with +/+, RQ/+, or RQ/RQ cells as indicated. Scale bar: 200 μm. **(D)** RQ/RQ OCLs are dramatically larger than +/+ OCLs grown on bone. M-CSF-treated splenocytes were seeded on bovine bone fragments, grown in the presence of RANKL, and stained for TRAP. Left: The average size (mean±SD) of OCLs was 1,151±54 μm^2 (+/+; n=353 cells) vs. 16,892±3,682 μm^2 (RQ/RQ; n=280 cells; $p<0.0001$ by Student's t-test). Right: The average sizes of the largest 5% of OCLs in either genotype was 4,207±217 μm^2 (+/+; n=17 cells) vs. 206,175±52,323 μm^2 (RQ/RQ; n=14 cells; $p<0.0001$ by Student's t-test). Note that the Y axis scale is logarithmic. **(E)** RQ/RQ OCLs express normal amounts of SNX10 protein. +/+, RQ/+ and RQ/RQ OCLs, grown in the presence of M-CSF (macrophages) or M-CSF and RANKL (osteoclasts) were analyzed by protein blotting for SNX10 expression, with actin as a loading control. Data shown are from line 43; homozygous R51Q SNX0 mice from line 87 produced identical results.

Fig 6: Giant OCLs of R51Q SNX10 homozygous mice exhibit structurally-abnormal or missing ruffled borders.

Spleen cells from +/+ and RQ/RQ mice were seeded on slices of bovine bone and grown in the presence of M-CSF and RANKL for 15 days. **(A)** Transmission electron microscopy (TEM) images of +/+ (left) and RQ/RQ (right) OCLs grown on bone. Top: Scale bars: 2 μm. Bottom: Enlarged images of boxed regions in top panels. Scale bar: 500 nm. Images are representative of a total of 17 +/+, 5 RQ/+, and 17 RQ/RQ cells examined. RQ/+ cells were indistinguishable from +/+ cells. b, bone **(B)** Similar to A, showing sections of mouse bones with endogenous OCLs. Mice examined were females aged 5 weeks. Top: Scale bars: 10 μm. Bottom: enlarged images of boxed regions in top panels. Scale bars: 1 μm. b, bone.

Figure 1

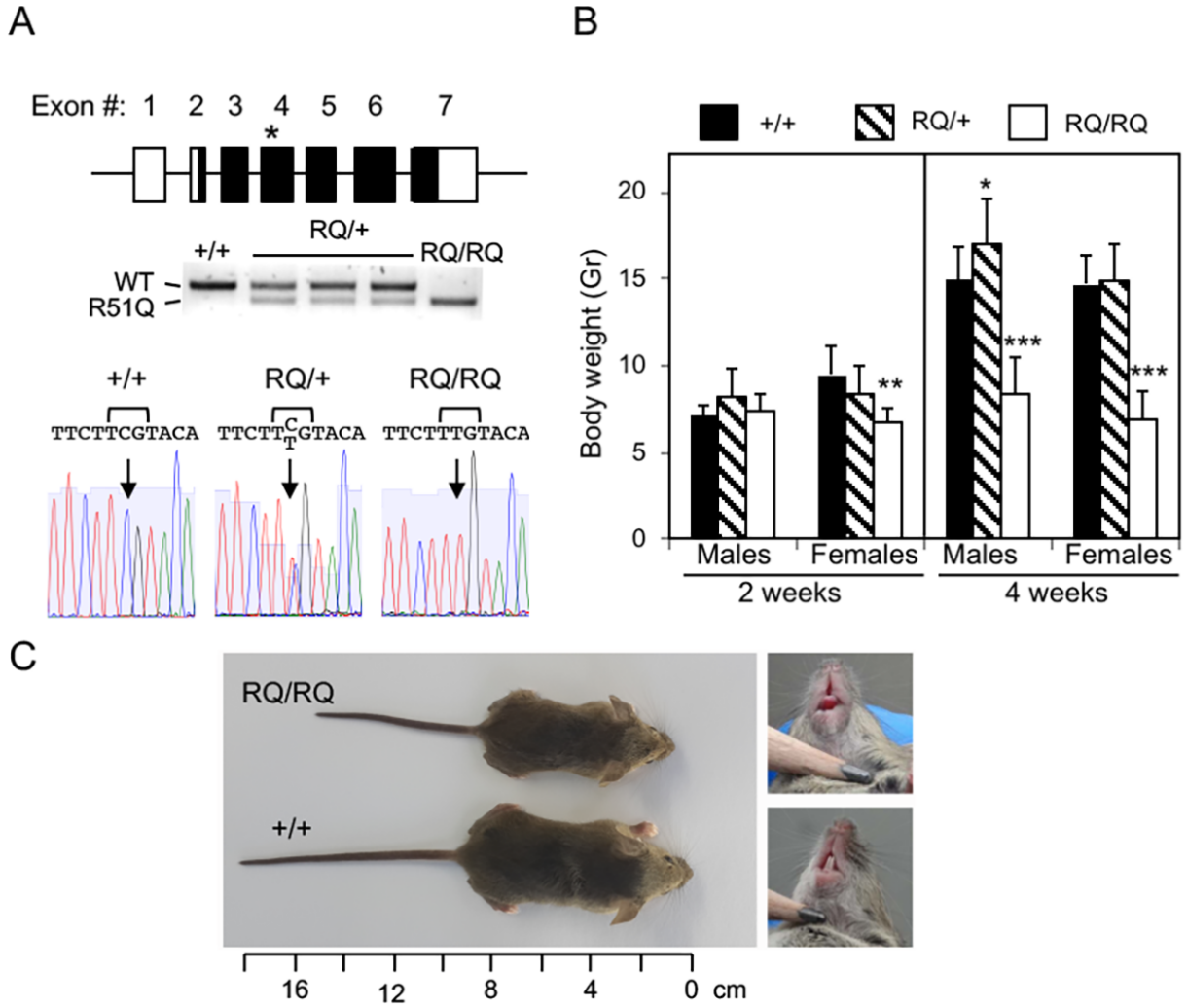
A
Exon #: 1 2 3 4 5 6 7
*
+/+
RQ/+
RQ/RQ
WT
R51Q
+/+
RQ/+
RQ/RQ
TTCTTCGTACA
TTCTTCTGTACA
TTCTTTGTACA
B
+/+
RQ/+
RQ/RQ
Body weight (Gr)
20
15
10
5
0
*
**
***
***
Males
Females
Males
Females
2 weeks
4 weeks
C
RQ/RQ
+/+
16
12
8
4
0 cm

Figure 2

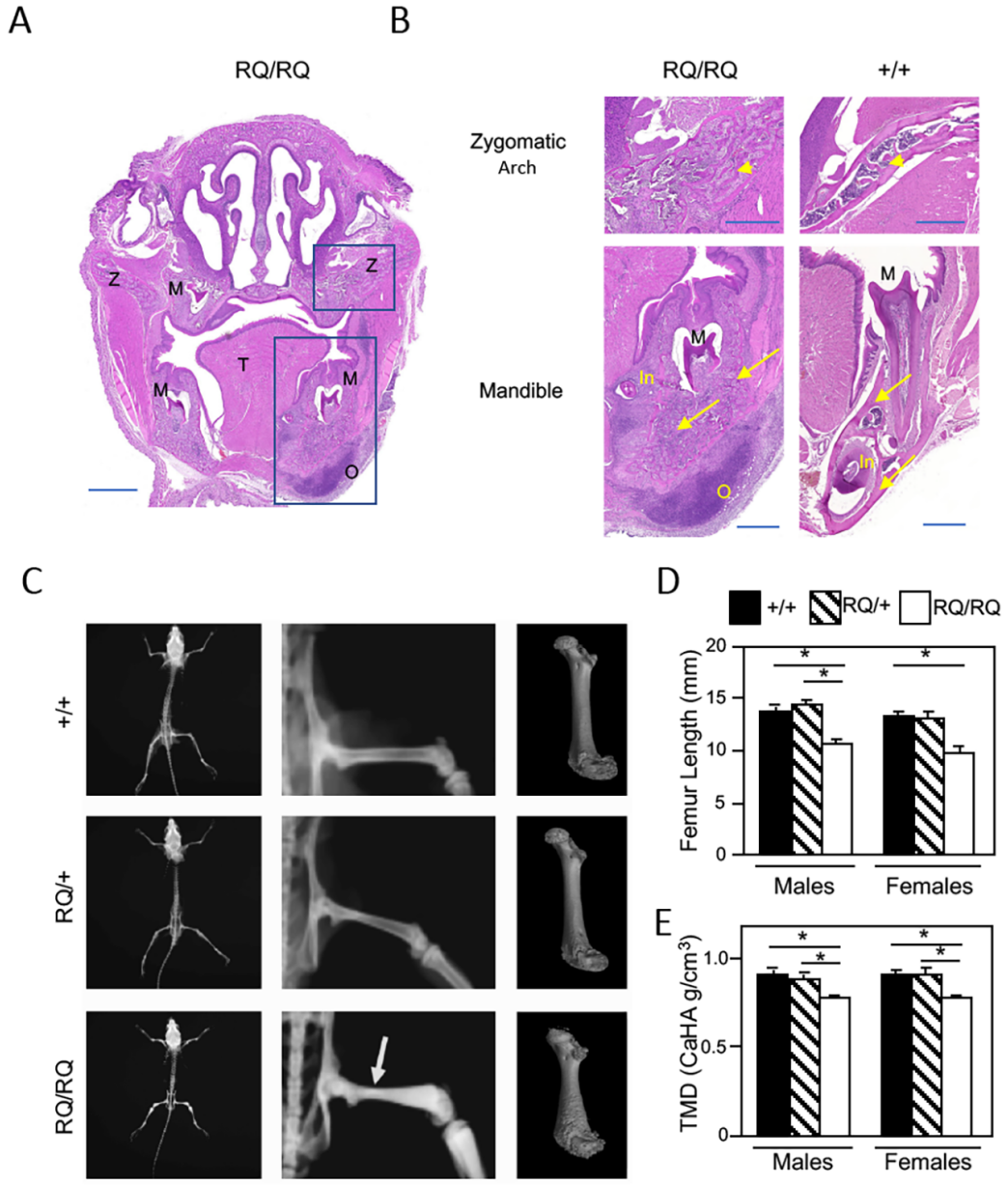
A
RQ/RQ
Z
M
T
M
M
Z
O
B
RQ/RQ
+/+
Zygomatic Arch
Mandible
M
In
O
M
In
C
+/+
RQ/+
RQ/RQ
D
+/+
RQ/+
RQ/RQ
Femur Length (mm)
20
15
10
5
0
Males
Females
E
TMD (CaHA g/cm3)
1.0
0.5
0
Males
Females

Figure 3

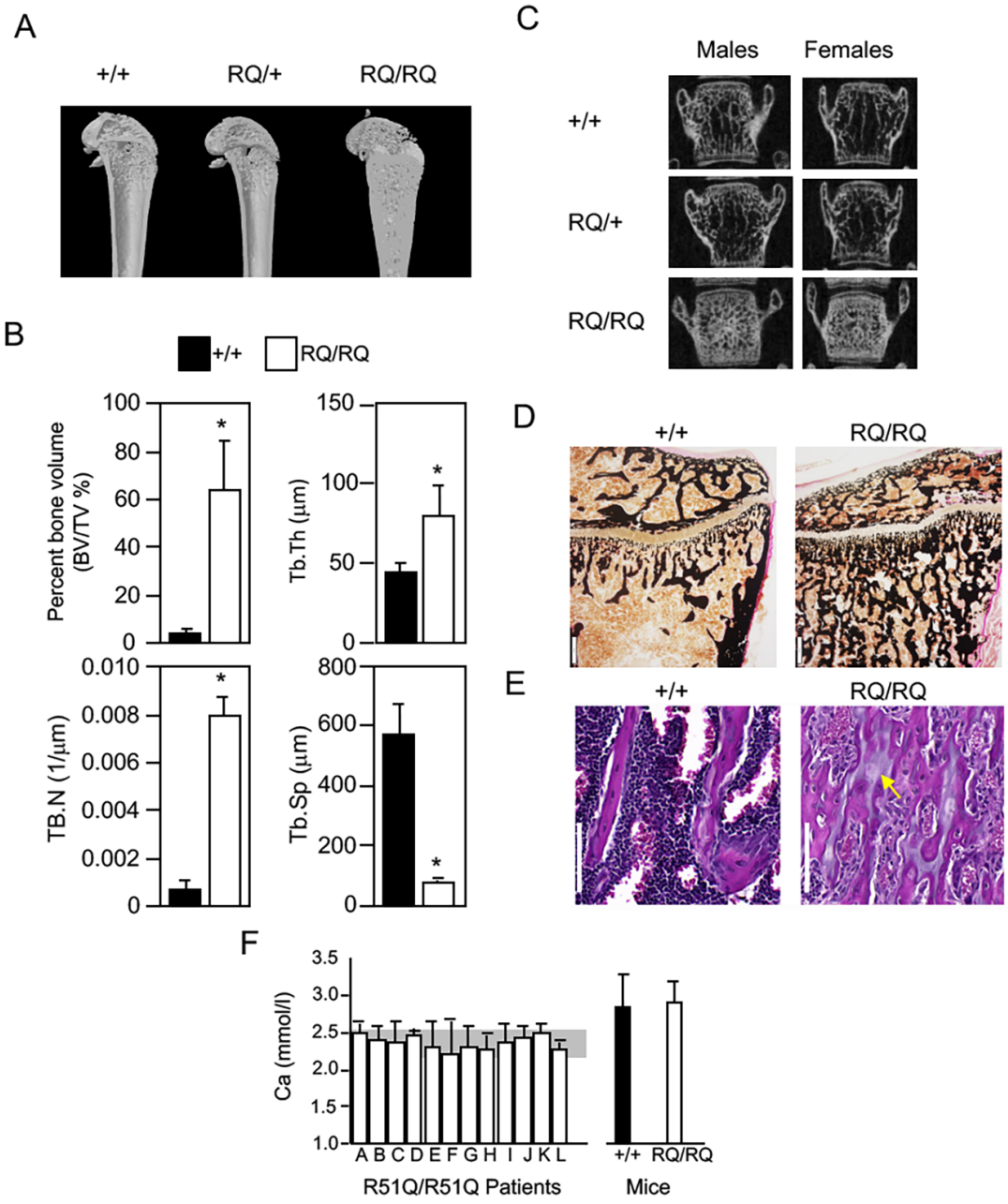
A
+/+
RQ/+
RQ/RQ
B
+/+
RQ/RQ
Percent bone volume (BV/TV %)
Tb.Th (µm)
TB.N (1/µm)
Tb.Sp (µm)
C
Males
Females
+/+
RQ/+
RQ/RQ
D
+/+
RQ/RQ
E
+/+
RQ/RQ
F
Ca (mmol/l)
A B C D E F G H I J K L
R51Q/R51Q Patients
+/+ RQ/RQ
Mice

Figure 4

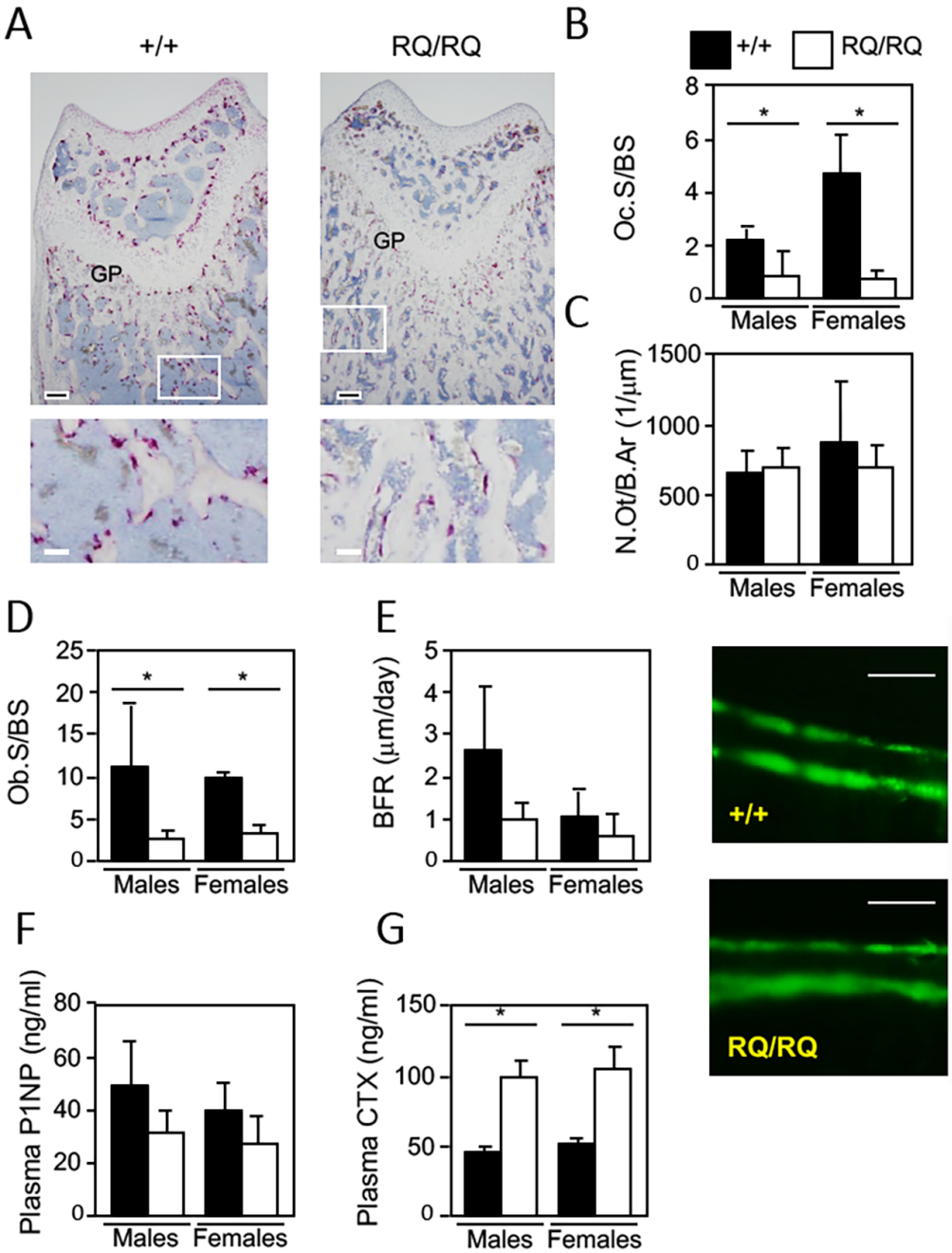
A
+/+
RQ/RQ
GP
GP
B
+/+
RQ/RQ
Oc.S/BS
8
6
4
2
0
*
*
Males
Females
C
N.Ot/B.Ar (1/µm)
1500
1000
500
0
Males
Females
D
Ob.S/BS
25
20
15
10
5
0
*
*
Males
Females
E
BFR (µm/day)
5
4
3
2
1
0
Males
Females
+/+
RQ/RQ
F
Plasma P1NP (ng/ml)
80
60
40
20
0
Males
Females
G
Plasma CTX (ng/ml)
150
100
50
0
*
*
Males
Females

Figure 5

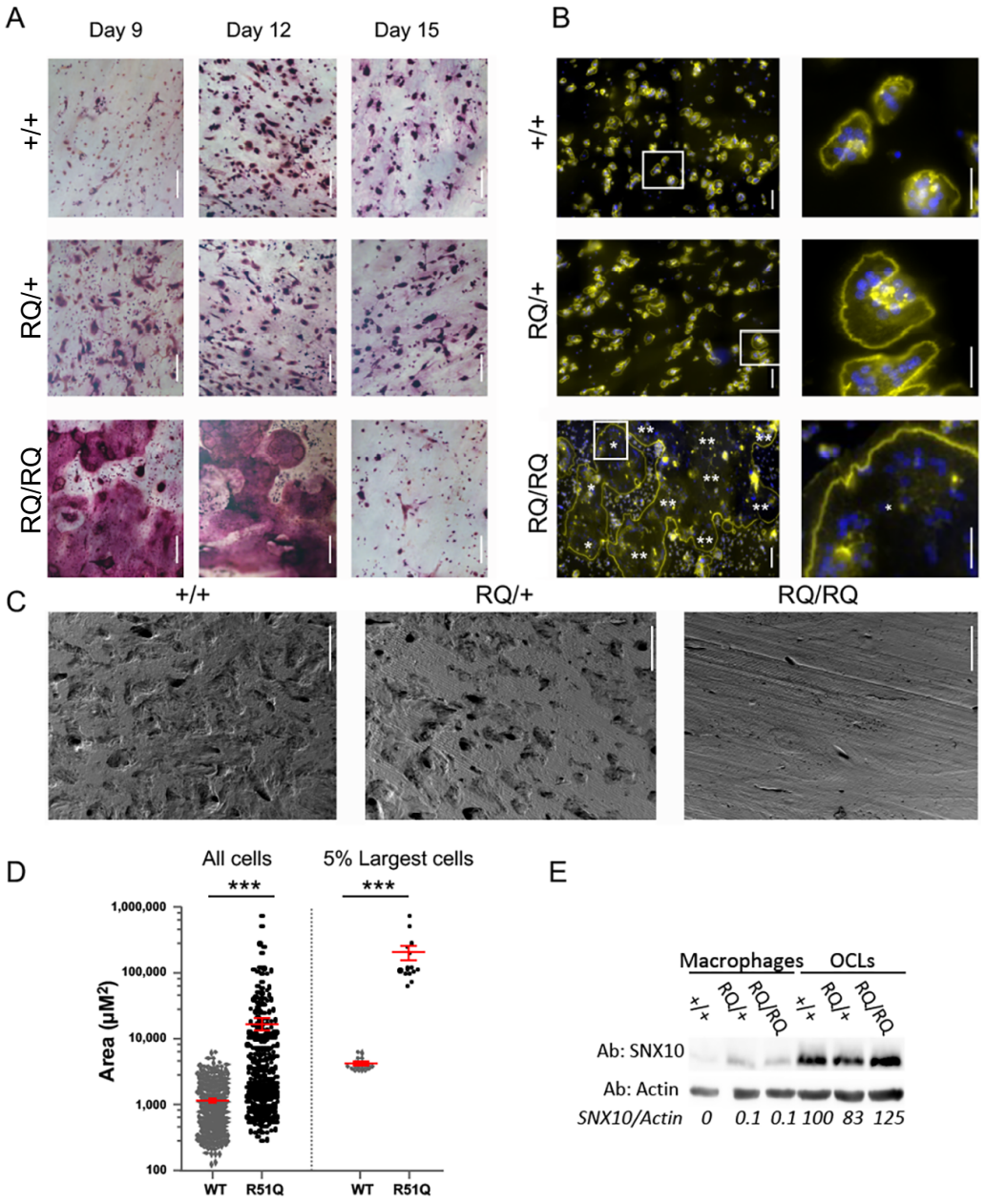
A
Day 9
Day 12
Day 15
+/+
RQ/+
RQ/RQ
B
+/+
RQ/+
RQ/RQ
C
+/+
RQ/+
RQ/RQ
D
All cells
5% Largest cells
***
***
Area (µM²)
1,000,000
100,000
10,000
1,000
100
WT
R51Q
WT
R51Q
E
Macrophages
OCLs
+/+
RQ/+
RQ/RQ
+/+
RQ/+
RQ/RQ
Ab: SNX10
Ab: Actin
SNX10/Actin 0 0.1 0.1 100 83 125
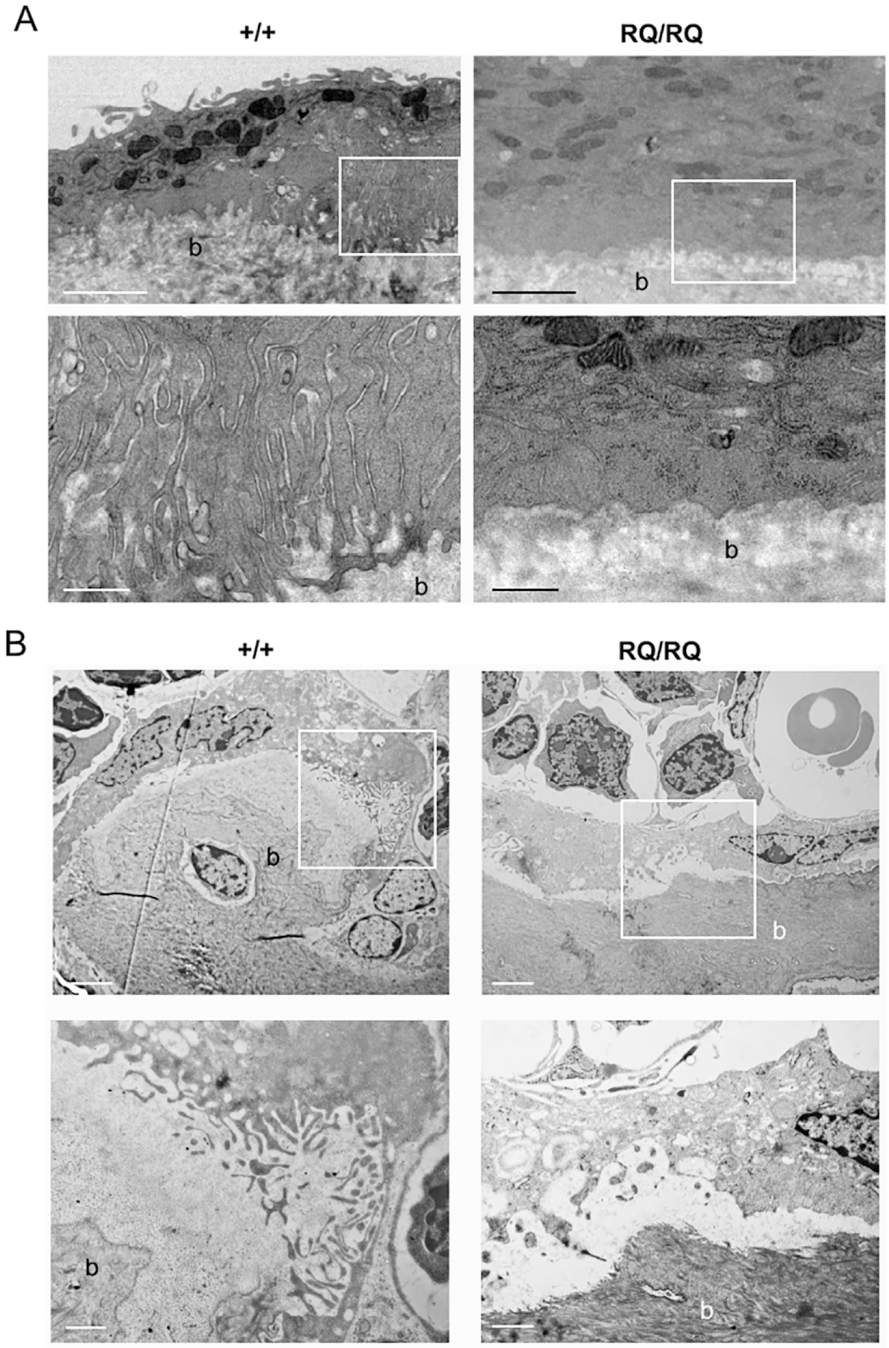
Figure 6